# A 3-D Computational Study of a Variable Camber Continuous Trailing Edge Flap (VCCTEF) Spanwise Segment

Upender K. Kaul* and Nhan T. Nguyen**
NASA Ames Research Center, USA.

Results of a computational study carried out to explore the effects of various elastomer configurations joining spanwise contiguous Variable Camber Continuous Trailing Edge Flap (VCCTEF) segments are reported here. This research is carried out as a proof-of-concept study that will seek to push the flight envelope in cruise with drag optimization as the objective. The cruise conditions can be well off design such as caused by environmental conditions, maneuvering, etc. To handle these off-design conditions, flap deflection is used so when the flap is deflected in a given direction, the aircraft angle of attack changes accordingly to maintain a given lift. The angle of attack is also a design parameter along with the flap deflection . In a previous 2D study,[1] the effect of camber was investigated and the results revealed some insight into the relative merit of various camber settings of the VCCTEF. The present state of the art has not advanced sufficiently to do a full 3-D viscous analysis of the whole NASA Generic Transport Model (GTM) wing with VCCTEF deployed with elastomers. Therefore, this study seeks to explore the local effects of three contiguous flap segments on lift and drag of a model devised here to determine possible trades among various flap deflections to achieve desired lift and drag results. Although this approach is an approximation, it provides new insights into the "local" effects of the relative deflections of the contiguous spanwise flap systems and various elastomer segment configurations. The present study is a natural extension of the 2-D study[1] to assess these local 3-D effects. Design cruise condition at 36,000 feet at free stream Mach number of 0.797 and a mean aerodynamic chord (MAC) based Reynolds number of $30.734 \times 10^6$ is simulated for an angle of attack (AoA) range of 0 to 6 deg. In the previous 2-D study,[1] the calculations revealed that the parabolic arc camber (1x2x3) and circular arc camber (VCCTEF222) offered the best L/D characteristics and minimum drag in cruise. In the present 3-D study, calculations show that for the same $C_l$, the 3-D circular arc camber wing segment produces the largest drag for a given lift, larger than either of the two 2-D configurations, as was also conjectured in the previous study.[1] This study indicates a wing stall around 4.5 deg angle of attack.

*Keywords:* Variable Camber Continuous Trailing Edge Flap (VCCTEF), Drag Optimization, Generic Transport Model.

* Applied Modeling and Simulations Branch, NASA Advanced Supercomputing (NAS) Division; Associate Fellow, AIAA

** Intelligent Systems Division; Associate Fellow, AIAA

## Nomenclature

$\alpha$ = angle of attack (AoA)
$C_l$ = lift coefficient (total or sectional)
$C_d$ = drag coefficient (total or sectional)
$C_p$ = pressure coefficient: $2(p - p_\infty) / \rho {V_\infty}^2$
$L$ = sectional lift
$D$ = sectional drag
$M$ = Mach number
$Re$ = Reynolds number
$M_\infty$ = free stream Mach number
$V_\infty$ = free stream Velocity
$\theta$ = Momentum thickness

# 1 Introduction

The aircraft industry has been responding to the need for energy-efficient aircraft by redesigning airframes to be aerodynamically efficient, employing light-weight materials for aircraft structures and incorporating more energy-efficient aircraft engines. Reducing airframe operational empty weight (OEW) using advanced composite materials is one of the major considerations for improving energy efficiency. Modern light-weight materials can provide less structural rigidity while maintaining sufficient load-carrying capacity. As structural flexibility increases, aeroelastic interactions with aerodynamic forces and moments can alter aircraft aerodynamics significantly, thereby potentially degrading aerodynamic efficiency.

Under the Advanced Air Vehicle Program (AAVP) of the NASA Aeronautics Research Mission Directorate, the Advanced Air Transportation Technologies (AATT) project is conducting multidisciplinary foundational research to investigate advanced concepts and technologies for future aircraft systems. A NASA study entitled "Elastically Shaped Future Air Vehicle Concept" was conducted in 2010[3,4] to examine new concepts that can enable active control of wing aeroelasticity to achieve drag reduction. This study showed that highly flexible wing aerodynamic surfaces can be elastically shaped in-flight by active control of wing twist and vertical deflection in order to optimize the local angle of attack of wing sections. Thus aerodynamic efficiency can be improved through drag reduction during cruise and enhanced lift performance during take-off and landing.

The study shows that active aeroelastic wing shaping control can have a potential drag reduction benefit. Conventional flap and slat devices inherently generate drag as they increase lift. The study shows that in cruise, conventional flap and slat systems are not aerodynamically efficient for use in active aeroelastic wing shaping control for drag reduction. A new flap concept, referred to as Variable Camber Continuous Trailing Edge Flap (VCCTEF) system, was conceived by NASA to address this need.[3] Initial study results indicate that, for some applications, the VCCTEF system may offer a potential pay-off in drag reduction that could provide significant fuel savings. Fig. 1 illustrates the VCCTEF deployed on the NASA generic transport model (GTM).

NASA and Boeing are currently conducting a joint study to develop the VCCTEF further under the research element Active Aeroelastic Shape Control (AASC) within the AATT project.[5,6] This study built upon the development of the VCCTEF system for the NASA Generic Transport Model (GTM),[7] employing light-weight shaped memory alloy (SMA) technology for actuation and three separate chordwise segments shaped to provide a variable camber to the flap. This cambered flap has potential for drag reduction as compared to a conventional straight, plain flap. The flap is also made up of individual 2-foot spanwise sections, which enable different flap settings at each flap spanwise position. This results in the ability to control the wing twist shape as a function of span, resulting in a change to the wing twist to establish the best lift-to-drag ratio (L/D) at any aircraft gross weight or mission segment. Current wing twist on commercial transports is permanently set for one cruise configuration, usually for a 50% loading or mid-point on the gross weight schedule. The VCCTEF offers different wing twist settings for each gross weight condition and also different settings for climb, cruise and descent, a major factor in obtaining best L/D conditions.

The second feature of VCCTEF is a continuous trailing edge. The individual 2-foot spanwise flap sections are connected with a flexible covering, so no breaks can occur in the flap platforms thus reducing excessive

vorticity generation. This reduces drag and airframe noise. This continuous trailing edge flap design combined with the flap camber result in lower drag increase during flap deflections. In addition, it also offers a potential noise reduction benefit.

In a previous paper,[1] a computational study was conducted to explore the two-dimensional viscous effects of a number of the VCCTEF configurations on lift and drag of GTM wing section at the wing planform break. The flow solver OVERFLOW was used to conduct this study. The results identified the most aerodynamically efficient VCCTEF configuration among the initial candidates.

A typical 3-D spanwise segment considered here consists of a spanwise three-flap system, two end baseline undeflected flaps connected by a circular arc VCCTEF222[1] in the center and two elastomer segments. Four spanwise elastomer shapes are considered. The first elastomer shape is defined by linearly stretching it between each baseline flap and the central circular arc VCCTEF, with an appropriate tangential contact between the elastomer and the two neighboring flap systems. The other three elastomer shapes are chosen using three different splines. The chosen 3-D spanwise wing segment is thought of as a central segment flanked on both sides by a number of similar 3-D segments. Therefore periodic boundary conditions are enforced at the two spanwise end stations. The linear elastomer shall be referred to as $config_1$ with configs 2 to 4 referring to elastomers with increasing curvature. The present 3-D work reveals the presence of streamwise vorticity aft of the trailing egde near the junction between the end baseline and the neighboring elastomer segments. Therefore, the deflection of contiguous flap segments should be held to a certain threshold value to avoid any adverse effects on flight performance. Also, various elastomer configurations were considered allowing assessment of their relative performance.

## 2 Computational Setup

A subset of the VCCTEF system shown in Fig. 2 is used as a 3-D computational configuration for a spanwise segment. Fig. 2 shows a schematic of the VCCTEF mounted on the trailing edge of a GTM wing. In this figure, we observe that the VCCTEF spans a subset of the wing span. The VCCTEF at the wing break station has an overall chord of 54 in. The VCCTEF profiles are depicted in Fig. 3, and a comparative plot of the four elastomer profiles is shown in Fig. 4, showing the linear and the three nonlinear elastomers. In the earlier companion study,[1] it was demonstrated that the two best configurations for cruise were the circular arc (VCCTEF222) and parabolic arc (VCCTEF123) configurations. Each digit in the 222/123 designation is the angle of the trailing edge segment. Therefore, in the present study, a 3-D segment is considered in which two baseline (retracted or undeployed flaps) configurations are connected to the circular arc configuration by two elastomer segments on either side of the VCCTEF222, thus connecting the baseline VCCTEF on the left and right with the circular arc VCCTEF222 in the middle.

A single-zone fine grid of 500x125x145 was choosen for the first two elastomer configurations. A single zone fine grid of 500x129x145 was chosen for the third elastomer configuration, and a single-zone fine grid of 500x141x145 was selected for the fourth elastomer configuration. The first grid index refers to the grid distribution around the wing section (airfoil section), the second index refers to the spanwise direction and the third to the body normal direction. These single zone grids were generated using the elliptic grid generator[8]. In the earlier 2-D study[1], it was determined that the 500x145 grid distribution was fine enough for the purpose of evaluating the lift and drag results in comparison with NACA0012 experimental results[9]. In the present study, an equally fine spacing in the spanwise direction was chosen, as mentioned above. Additionally, a finer grid spacing of 213 points for the linear elastomer configuration and 229 points for the nonlinear elastomer ($config_4$) configuration in the spanwise direction was used. The results show very little difference between these two fine grids in the spanwise direction. This will be shown in the discussion of grid sensitivity study in the section on Simulation Results below.

A typical 3-D spanwise segment is shown in Figs. 5(a,b). The circular arc flap, VCCTEF222, is shown in the middle in blue flanked by two baseline flaps shown in red on either side. The elastomers joining the circular arc and the baseline flaps are shown in green. Sectional results will be presented at sections AA, BB and CC. These sections are shown in Fig. 5(b). Periodic boundary conditions are enforced at the two end spanwise stations. Even though this computational setup is approximate, it will provide some insights into the local effects of the components of this VCCTEF subsystem.

Representative grids are shown in Fig. 6(a-c). Fig. 6(a) shows the grid point distribution on a section of

the geometry of the 3-D model. Appropriate clustering of grid points is achieved in the spanwise direction around the transitions between the baseline, elastomer and VCCTEF222 segments. Fig. 6(b) shows a section of a volume grid over the section CC as shown in Fig. 5(b), and Fig. 6(c) shows a section of a volume grid over the section BB.

The flow conditions used correspond to cruising Mach number of 0.797 and Reynolds number of $30.7x10^6$, with $\alpha = [0, 1, 2, 3, 4, 5, 6]$ degree. The free stream $M_\infty$ is 0.797, and Mach number normal to the leading edge is 0.7. The OVERFLOW solver was used in a time-accurate mode with an upwind scheme and a symmetric successive over-relaxation (SSOR) algorithm with sub-iterations. Also, simulations were conducted using OVERFLOW in steady mode, which ran two orders of magnitude faster than the time-accurate mode. Both sets of simulations yield about the same steady state result. In the present OVERFLOW simulations, the flow was simulated up to 6 deg angle of attack (AoA).

# 3 Simulation Results

Cruising flight of a GTM spanwise wing segment was simulated using OVERFLOW with the Spalart-Allmaras (SA)[2] turbulence model, based on the best performance of the SA turbulence model in the previous companion study.[1] Fig. 7(a) shows the $C_l - \alpha$ plots corresponding to the four elastomer configurations (refer Fig. 4) for the whole 3-D segment. For added comparison, the 2-D results[1] for the baseline and circular arc configurations are also shown. The present 3-D results show increased lift compared to the 2-D baseline up to $\alpha$ of about 4 deg, as a result of the deflected flap. As the stall regime is approached, the 3-D results show lower $C_l$ for a given angle of attack than both the 2-D configurations. Wing stall occurs around $\alpha = 4.5$ deg for all four elastomer configurations. Results of grid sensitivity are shown in Fig. 7(b) for the linear elastomer and one of the nonlinear elastomer configurations. As the spanwise grid is refined from 125 grid points to 213 grid points for the linear elastomer configuration, $C_l$ shows practically the same result for $\alpha$ = 0.0, 2.0, 3.0, 3.5, 4.0 and 4.5 deg. Similarly, for the nonlinear elastomer configuration ($config_4$), $C_l$ is practically the same at $\alpha$ = 0.0, 2.0, 3.0, 3.5, 4.0 and 4.5 deg. Overall, two grid resolutions used in this study give practically the same result at the stall angle and in the pre-stall regimes. Since we are doing a steady RANS study here, calculations in the post-stall regime are not of high fidelity, since that requires an unsteady RANS to resolve the highly unsteady flow field.

The variation of $C_d$ with $\alpha$ is shown in Fig. 8. All four 3-D configurations show a slightly higher drag than the 2-D baseline configuration and smaller drag than the circular arc configuration for all $\alpha$ tested here. Both 2-D baseline and the 3-D configurations predict drag lower than that corresponding to the 2-D circular arc (VCCTEF222).

The corresponding drag polar is shown in Fig. 9(a). The drag polar shows that for a given value of $C_l$, all four 3-D configurations give higher drag than either of the 2-D configurations. Corresponding L/D characteristics are shown in Fig. 10. The 3-D configurations show a L/D variation with $C_l$ at a level below that of the 2-D configurations, even though the lift produced by the 3-D segment at a given angle of attack is higher than the 2-D baseline configuration. The reason for this is that the drag of the 3-D segment is higher than the 2-D baseline configuration, as shown in Fig. 8(a). Corresponding results for grid sensitivity of drag polars are shown in Fig. 9(b). Similar behavior of the drag polar results is shown as for the $C_l$ results, i.e., grid independence has been achieved with the two grids used here. Therefore, the remaining results shown below correspond to the first grid used.

Fig. 11(a,b,c) shows sectional $C_p$ variation for $\alpha = 4.5$ deg with the first grid at the three spanwise sections AA, BB and CC (refer to Fig. 5) corresponding to the left baseline, left elastomer and the middle circular arc segments, respectively. The $C_p$ variation corresponding to all the four elastomer configurations is practically the same at the three sections, with slight difference for $config_2$. Small blips around $x = 0.7$ at the sections BB and CC are due to the geometric transition between the main wing and the flaps involving slight discontinuity in slope. These are absent for the section AA since it is the baseline flap. The sectional $C_p$ distribution indicates a similar trend as the $C_l$ - $\alpha$ curve shown in Fig. 7 that the present elastomer configurations all contribute to lift somewhere between the 2-D results for baseline and VCCTEF222.

For a clearer comparison, sectional $C_p$ variation for $\alpha = 4.5$ deg is shown in Fig. 12 for $config_4$ and the 2-D results for baseline and VCCTEF222 configurations. Results for all the three sections, AA, BB and CC, are shown. There is very little variation in $C_p$ up to $x|approx$ 0.78, and then section CC tends to produce

higher $C_p$ than section BB, which in turn produces higher $C_p$ than section AA. It may be noted here that the geometric transition begins at $x \approx 0.7$, downstream of which we see these variations. Again, in agreement with results shown in Fig.7(b), Fig. 12 also predicts Cp from $config_4$ to be more than the baseline $C_p$ and less than the $C_p$ predicted by VCCTEF222.

The sectional lift and drag are calculated on thin strips at sections AA, BB and CC. Let the width of the thin strip in the spanwise direction be $\Delta y$. Then sectional lift and drag are calculated as

$$C_l = 2.0 * L/(\rho(V_\infty)^2 * \Delta y * c)$$

$$C_d = 2.0 * D/(\rho(V_\infty)^2 * \Delta y * c)$$

where L and D are the total lift and drag, respectively, calculated over the thin strip of area, $\Delta y * c$, at sections at AA, BB and CC and c is the mean aerodynamic chord. Typically, $\Delta y$ is of the order of 0.5 percent of the MAC.

The $C_p$ distribution over the entire 3-D wing segment with the linear elastomer configuration is shown in Fig. 13. These results correspond to the stall angle, $\alpha = 4.5$ deg. This figure provides an expected picture of the pressure differential between the suction and pressure sides of the wing segment

To investigate case of $config_4$ further, a particle trace visualization is shown in Fig. 14. Fig. 14(a) shows the trace of particles released near the trailing edge above the upper surface of $config_4$ for $\alpha = 4.5$ deg. It is shown that the flow moves upstream in this region near the surface of the wing. There are two distinct vortical flow regions on either side of the VCCTEF222 flap. The first one, a smaller region, shown in red is defined by particles released on the left baseline segment and part of the left elastomer segment, and the second one, a larger region, shown in green is defined by particles released on the remaining part of the left elastomer segment and left half of the VCCTEF222 segment. Similar situation is observed on the right half of the 3-D segment. It may be noted that the particles very near the surface do not move much. It is the particles that are released about 1/8th of MAC above the surface that highlight these vortical flow regions. Fig. 14(b) shows a zoomed-in view of the vortical flow pattern on the left half of the 3-D segment. This is an interesting picture of 3-D flow separation.

Particle trace visualization for $config_4$ at $\alpha = 2$ deg. is quite different. With the same set of particles released as in the case of $config_4$, the flow trace is minimal, as shown in Fig. 15. Flow particles stay close to the trailing edge without any movement toward the upstream direction, indicating that at $\alpha = 2$ deg., there is very little flow separation. It may be noted that flow along the underside of the 3-D segment near the trailing edge leaves the wing without any separation.

# 4 Concluding Remarks

A study to address the local effects of four elastomer configurations on a 3-D VCCTEF spanwise segment was carried out. The 3-D segment is a model that simulates a flow scenario that is not typical of a design cruise $C_l$, but that challenges the flight envelope to maintain a design $C_l$, and it provides some insight into the local flowfield over the considered 3-D segment. Since the technology to do a full 3-D viscous simulation of the GTM wing with VCCTEF and elastomers deployed is yet under development, the approach adopted here is an interim approach to analyze the local flowfield over the 3-D segment. Three nonlinear elastomer configurations and one linear elastomer configuration were considered. A 3-D VCCTEF spanwise wing segment was selected comprising of two baseline VCCTEF segments on either side of a middle circular arc VCCTEF222 segment, connected by an elastomer segment each on either side of the VCCTEF222 segment. Periodic boundary conditions are imposed in the spanwise direction. Two main conclusions are drawn from the present study. First, all the elastomer configurations considered indicate that for the angle of attack range between 0 and 6 degrees, even though the lift produced by the 3-D segment is consistently larger than that produced by the 2-D baseline, the $L/D$ characteristics of the 3-D segment are worse than the 2-D baseline and the 2-D circular arc. This is due to the larger drag predicted for the 3-D segment than that due to either of the two 2-D configurations. All the four elastomer configurations considered reflect about the same $L/D$ characteristics.

# 5 Acknowledgements

The authors would like to thank the NASA Aeronautics Research Mission Directorate (ARMD) Fixed Wing Project under the Fundamental Aeronautics Program for providing the funding support of this work. The authors wish to acknowledge Boeing Research and Technology for their collaboration with NASA under NASA contract NNL11AA05B task order NNL11AD25T entitled "Development of Variable Camber Continuous Trailing Edge Flap System." The first author's communication with Pieter Buning on OVERFLOW is thankfully acknowledged.

# 6 References

[1]Kaul, U. K. and Nguyen, N. T., "Drag Optimization Study of Variable Camber Continuous Trailing Edge Flap (VCCTEF) Using OVERFLOW," AIAA 2014-2444, 32nd Applied Aerodynamics Conference, Atlanta, GA, June 2014

[2]Spalart, P. R., and Allmaras, S. R., "A One-Equation Turbulence Model for Aerodynamic Flows," AIAA 92-0439, AIAA 30th Aerospace Sciences Meeting and Exhibit, Reno, NV , January 1992.

[3]Nguyen, N., "Elastically Shaped Future Air Vehicle Concept," NASA Innovation Fund Award 2010 Report, October 2010, Submitted to NASA Innovative Partnerships Program.

[4]Nguyen, N., Trinh, K., Reynolds, K., Kless, J., Aftosmis, M., Urnes, J., and Ippolito, C., "Elastically Shaped Wing Optimization and Aircraft Concept for Improved Cruise Efficiency," AIAA Aerospace Sciences Meeting, AIAA-2013-0141, January 2013.

[5]Boeing Report No. 2012X0015, "Development of Variable Camber Continuous Trailing Edge Flap System," October 4, 2012.

[6]Urnes, J., Nguyen, N., Ippolito, C., Totah, J., Trinh, K., and Ting, E., "A Mission Adaptive Variable Camber Flap Control System to Optimize High Lift and Cruise Lift to Drag Ratios of Future N+3 Transport Aircraft," AIAA Aerospace Sciences Meeting, AIAA-2013-0214, January 2013.

[7]Jordan, T. L., Langford, W. M., Belcastro, C. M., Foster, J. M., Shah, G. H., Howland, G., and Kidd, R., "Development of a Dynamically Scaled Generic Transport Model Testbed for Flight Research Experiments," AUVSI Unmanned Unlimited, Arlington, VA, 2004.

[8]Kaul, U. K., "Three-dimensional elliptic grid generation with fully automatic boundary constraints," J. Comput. Physics, 229 (2010), pp. 5966-5979, also AIAA Paper 2009-3994, 19th AIAA Computational Fluid Dynamics, 22-25 June 2009, San Antonio, Texas

[9]Maksymiuk, C. M. and Pulliam, T. H., "Viscous Transonic Airfoil Workshop Results using ARC2D," AIAA Paper 87-0415, AIAA 25th Aerospace Sciences Meeting, Reno, NV, January 1987.

# 1 Figures

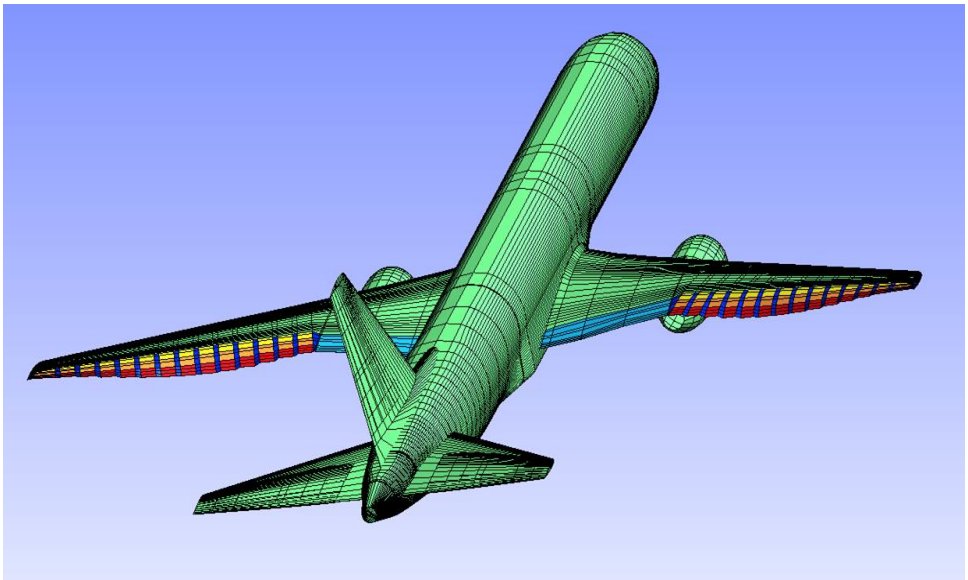

Figure 1: VCCTEF deployed on the generic transport model (GTM).

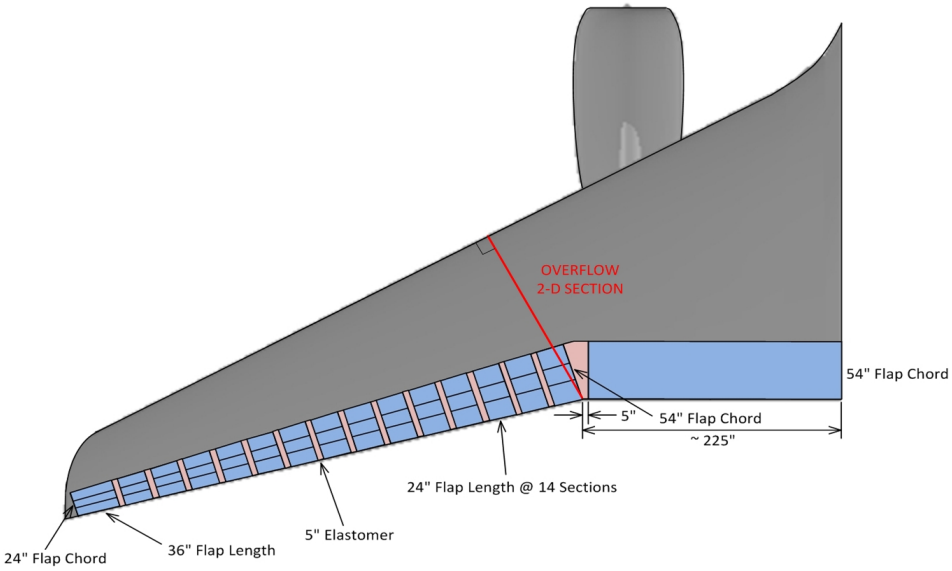


Figure 2: NASA/Boeing VCCTEF Configuration.

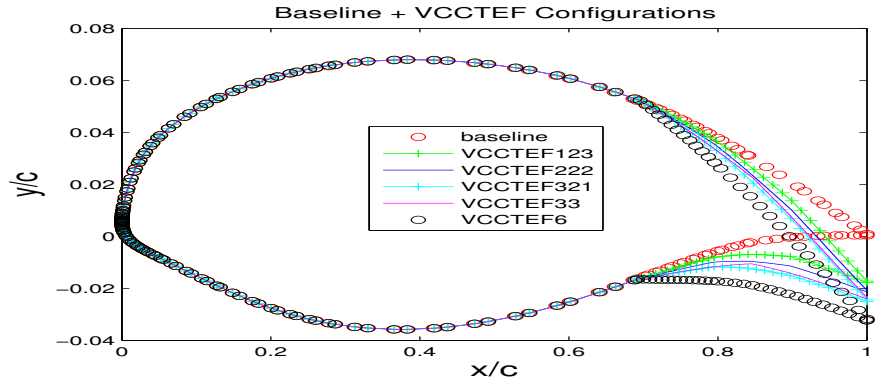


Figure 3: Different VCCTEF configurations and baseline configuration (VCCTEF retracted); figure taken from Ref. 1

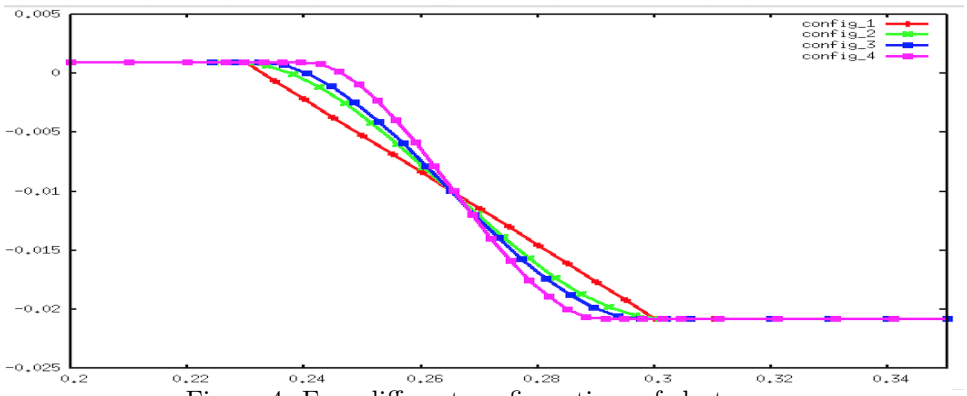


Figure 4: Four different configurations of elastomer

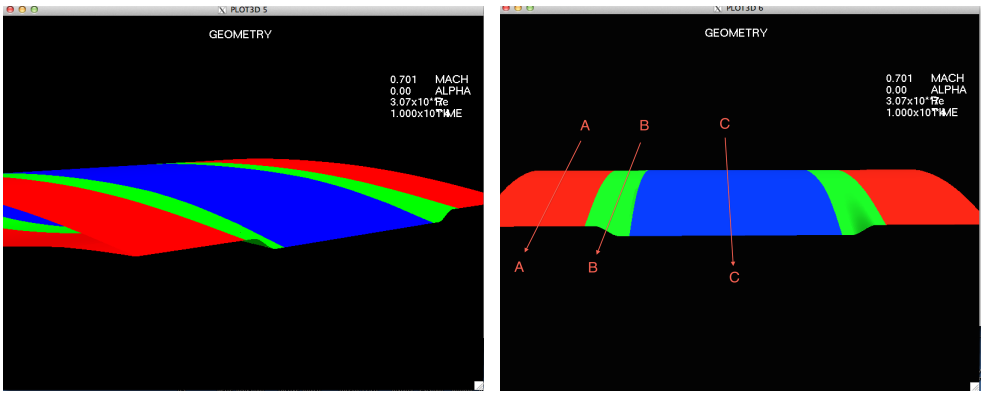


Figure 5: Two perspective views of a typical 3-D spanwise VCCTEF wing segment; $x$: chordwise; $y$: spanwise; $z$: vertical direction

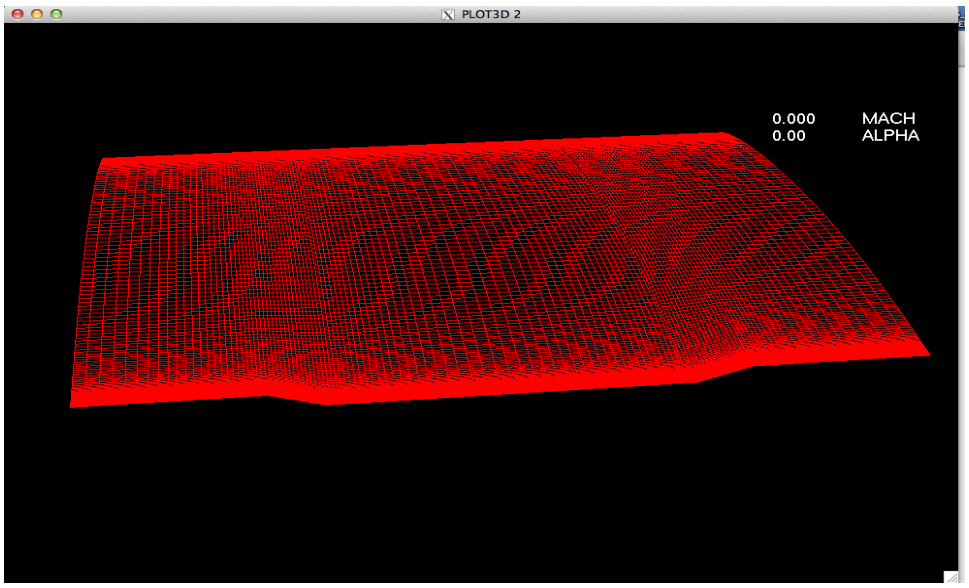


(a) Geometry

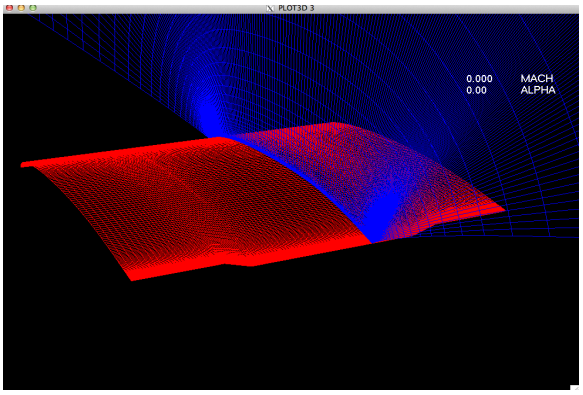


(b) Volume grid over section CC

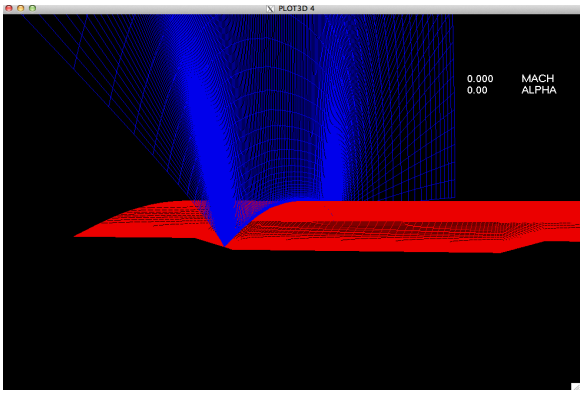


(c) volume grid over section BB

Figure 6: Perspective views of model geometry and representative grids

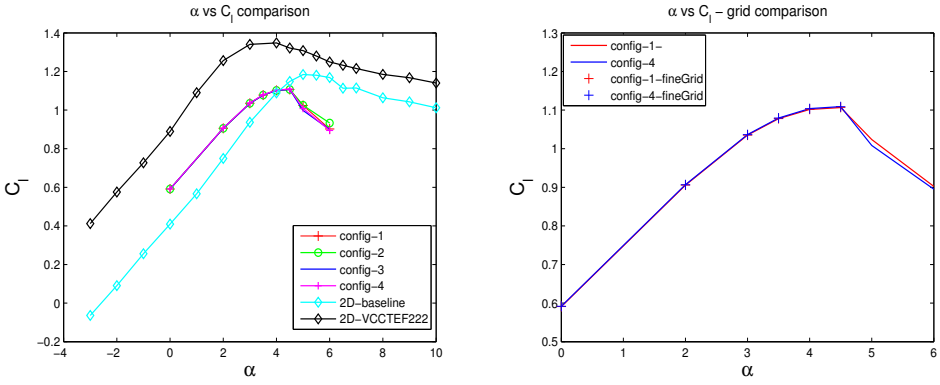


(a) (b) grid sensitivity

Figure 7: Lift curve: $C_l - \alpha$

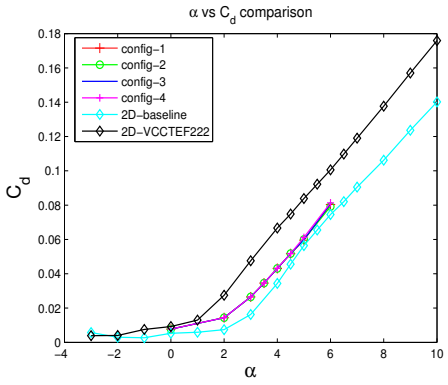


Figure 8: Drag curve: $C_d - \alpha$

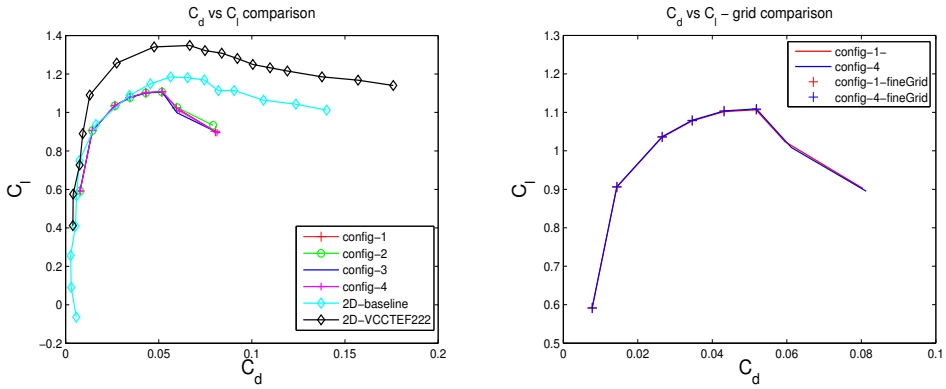


(a) (b) grid sensitivity

Figure 9: Drag polar: $C_l - C_d$

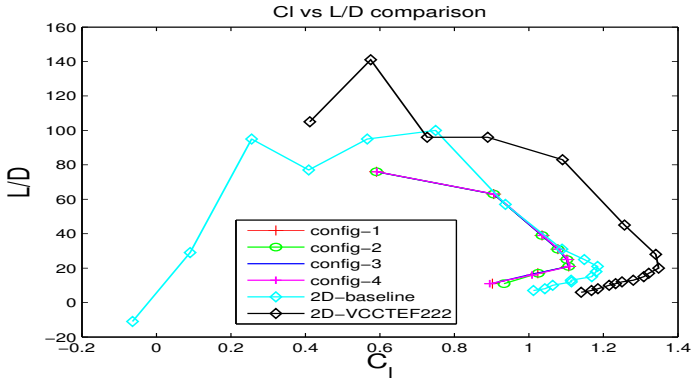


Figure 10: $L/D - \alpha$ curve

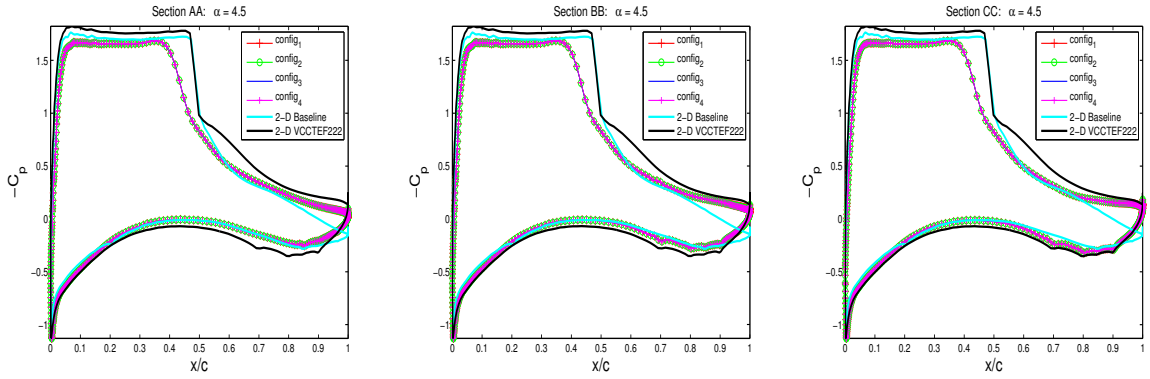


Figure 11: Sectional $C_p$ variation

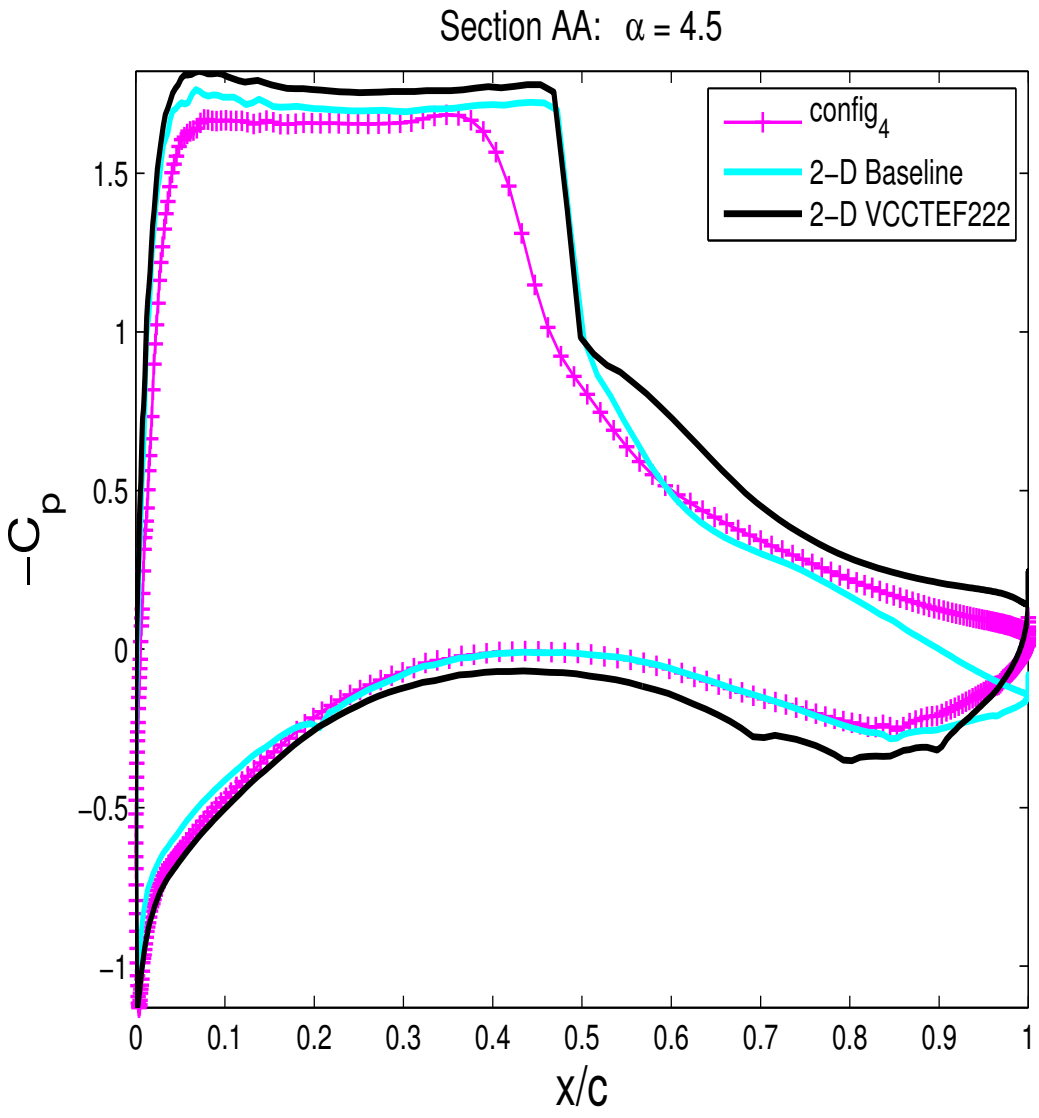


Figure 12: Sectional $C_p$ variation at AA, BB, CC: comparison of $config_4$ with 2-D

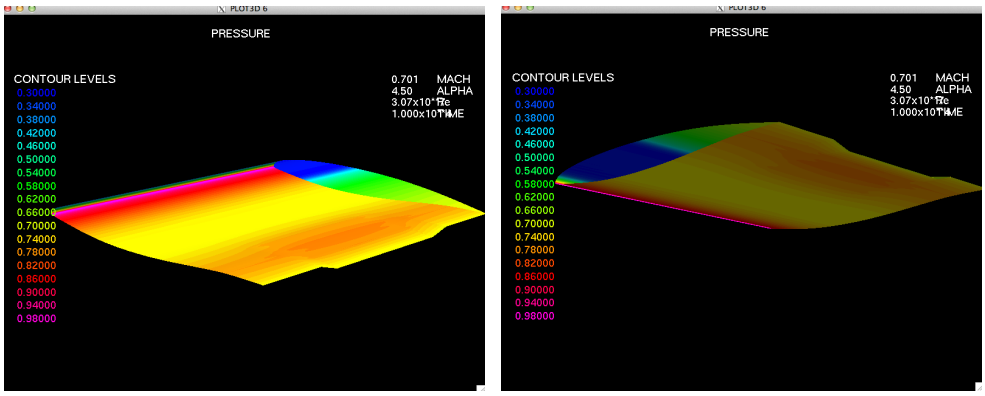


(a) Lower surface (b) Upper surface

Figure 13: Linear elastomer: pressure distribution; $\alpha = 4.5$ deg

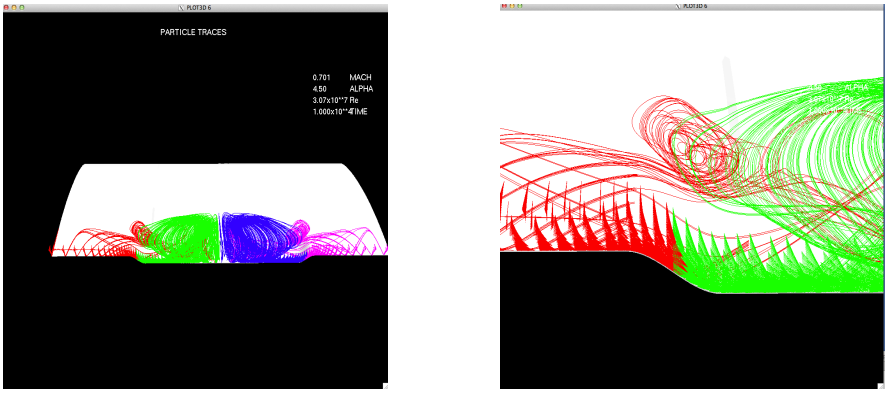


(a) overall vortical pattern (b) closer view on the left side

Figure 14: Particle trace visualization of flow above the upper surface: nonlinear elastomer ($config_4$), $\alpha = 4.5$ deg

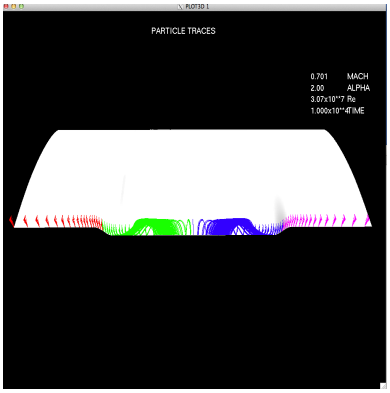


Figure 15: Particle trace visualization of flow above the upper surface: nonlinear elastomer ($config_4$), $\alpha = 2$ deg